


Examination of coexistence of symmetric mass and asymmetric charge distributions of fission fragments

H. Paşca 

Joint Institute for Nuclear Research, 141980 Dubna, Russia
and “Babeş-Bolyai” University, Faculty of Physics, 400084 Cluj-Napoca, Romania

A. V. Andreev and G. G. Adamian 

Joint Institute for Nuclear Research, 141980 Dubna, Russia

N. V. Antonenko

Joint Institute for Nuclear Research, 141980 Dubna, Russia
and Tomsk Polytechnic University, 634050 Tomsk, Russia



(Received 4 March 2020; accepted 14 May 2020; published 3 June 2020; corrected 24 September 2020)

Using the improved scission-point model, the mass and charge distributions of fission fragments of the compound nuclei $^{180,182,190,198}\text{Hg}^*$ and $^{202}\text{Pb}^*$ formed in complete fusion reactions $^{36}\text{Ar} + ^{144}\text{Sm}$, $^{40}\text{Ca} + ^{142}\text{Nd}$, $^{36}\text{Ar} + ^{154}\text{Sm}$, $\alpha + ^{194}\text{Pt}$, and $^{48}\text{Ca} + ^{154}\text{Sm}$ are studied and compared with available experimental data. The transition is explained from the mass-asymmetric distribution in fissioning $^{180,182,190}\text{Hg}^*$ to the mass-symmetric distribution found in fissioning $^{198}\text{Hg}^*$ and $^{202}\text{Pb}^*$. The retention of the asymmetric mass distributions is treated in the case of fissioning $^{180,182,190}\text{Hg}^*$ with increasing excitation energy. In the fissioning $^{198}\text{Hg}^*$ and $^{182}\text{Hg}^*$, completely different shapes are predicted for charge and mass yields.

DOI: [10.1103/PhysRevC.101.064604](https://doi.org/10.1103/PhysRevC.101.064604)

I. INTRODUCTION

The fission process remains one of the most interesting puzzles of modern physics, despite several decades of experimental and theoretical investigations. As known from the measured data, the charge and mass distributions of preactinides are symmetric while mass- and charge-asymmetric fragmentations are favored in nuclei heavier than thorium, U–Cf [1]. The fissioning nuclei ^APa and ^ATh with $A \leq 226$ ($A > 226$) and $A = 226$ display a single-peaked (two-peaked) and triple-peaked charge distribution, respectively. In general, the asymmetry of distribution is attributed to the shell effects in the fissioning nucleus or fission fragments. The closed spherical shells, like the ones found in the vicinity of Sn ($Z = 50$, $N = 82$), or/and deformed neutron shells (e.g., $N = 88$) have a large influence on the potential-energy landscape, creating minima that favor asymmetric divisions of the parent nucleus. There is a longstanding opinion that the competition between symmetric and asymmetric fission modes is mainly related to the deformed shells [2]. However, in neutron-deficient ^{180}Hg the asymmetric mass distribution of fission fragments was unexpectedly observed in Ref. [1]. This is an unusual behavior since the original prediction was that the symmetric division would be even more pronounced due to the $N = 50$ shell in the $^{90}\text{Zr} + ^{90}\text{Zr}$ fragmentation.

The evolution of mass and charge distributions of fission fragments with excitation energy is also an important aspect in fission studies. The transition from an asymmetric distribution to a symmetric one with increasing excitation

energy is attributed to a weakening of the shell effects. However, in the cases of neutron-induced fission of ^{232}Th and ^{238}U , the recent experimental data have shown that the mass distributions maintain the asymmetric shape even at neutron energies of $E_n \sim 60\text{--}70$ MeV [3–5]. Asymmetric shapes of the mass distribution resulting from the fission of highly excited nuclei $^{237\text{--}240}\text{U}$, $^{239\text{--}242}\text{Np}$, and $^{241\text{--}244}\text{Pu}$ (at excitation energies $E_{\text{CN}}^* \sim 60\text{--}70$ MeV), originating from the transfer reaction $^{18}\text{O} + ^{238}\text{U}$ at $E_{\text{lab}} = 157.5$ MeV, have been experimentally observed in Ref. [6]. The same effect has been observed in Refs. [7,8]. The presence of a strong asymmetric component in the fission of ^{244}Cm at $E_{\text{CN}}^* = 23$ MeV and ^{250}Cf at $E_{\text{CN}}^* = 46$ MeV has been recently observed in Refs. [9,10]. Furthermore, the experimental mass distribution of fission fragments of the compound nuclei (CN) $^{180,182,190}\text{Hg}^*$ and $^{178}\text{Pt}^*$ formed in complete fusion reactions $^{36}\text{Ar} + ^{142}\text{Nd}$, $^{144,154}\text{Sm}$ and $^{36}\text{Ar} + ^{142}\text{Nd}$ at different bombarding energies [11–13] showed a weak change of the asymmetric shape of respective distributions, even though large excitation energies ($E_{\text{CN}}^* = 60\text{--}75$ MeV) and angular momenta ($L = 59\text{--}74$) have been involved. All these experimental data are in contrast with the belief that the shell effects wash out rather rapidly with increasing excitation energy. At these large excitation energies, the shell effects are expected to be washed out, and the nucleus is supposed to leave with a dominant symmetric mode, in contrast to the experiments. Thus, the statement that the fast melting of shell effects with excitation energy always results in the fissioning nucleus having a dominant symmetric mode

is not completely correct. The possible reason(s) for this could be the underestimation of the roles of shell and/or macroscopic effects. Because the shell effects are very important for the description of fission properties of heaviest actinides, it is interesting to study the excitation energy dependence of the fission observables in these nuclei. Note that the multichance fission at $E_{\text{CN}}^* \geq 50$ MeV cannot explain [14] the presence of the asymmetric mode in the experiments mentioned.

In the present paper we will study the evolution of charge and mass distributions of fission fragments with increasing excitation energy in the fissioning even-even $^{180,182,190,198}\text{Hg}$ isotopes. Our aim is to predict the charge and mass distributions at large excitation energies. The fission observables are described using the improved scission-point model [15–19]. The statistical scission-point model [15–19] relies on the assumption that statistical equilibrium is established at the touching configuration of fragments where the observable characteristics of the fission process are formed. The reliability of this conclusion is supported by a good description of various experimental data (mass, charge, kinetic-energy distributions, and neutron multiplicity) with the scission-point-type models [15–28].

II. MODEL

The most important step of the scission-point model is the calculation of the potential energy of the dinuclear system (DNS) as a function of charge Z_i , mass A_i , deformations β_i (the ratios between the major and minor semiaxes of the fragments) of the two fragments, and internuclear distance R between them. The index i designates the light (L) or (H) heavy fragment. The scission configuration is imagined as two axially deformed and uniformly charged ellipsoids—the nascent fragments. The two nuclei are fully formed and possess all the features of isolated nuclei, e.g., binding energies, according to the separability principle [29], and mutually interact through the nuclear and Coulomb forces. Their orientation is frozen to a tip-to-tip configuration, which provides the minimum of interaction energy. Owing to the repulsive nature of the Coulomb interaction V^C and rotational energy V^R , and attractive nature of the nuclear interaction V^N , a potential pocket is formed in R coordinates with a minimum at $R = R_m$ which roughly corresponds to a separation of 0.5–1 fm between the tips of the fragments, depending on the mass $A_{L,H}$ and charge $Z_{L,H}$ numbers, and deformations $\beta_{L,H}$. Because the model assumes statistical equilibrium at the scission point, one can reduce the complexity of the problem by fixing the internuclear distance at the bottom of the potential pocket ($R = R_m$). Then, the potential energy

$$\begin{aligned} U(A_i, Z_i, \beta_i, R_m, L) &= U_L^{\text{LD}}(A_L, Z_L, \beta_L, E_L^*) + \delta U_L^{\text{shell}}(A_L, Z_L, \beta_L, E_L^*) \\ &+ U_H^{\text{LD}}(A_H, Z_H, \beta_H, E_H^*) + \delta U_H^{\text{shell}}(A_H, Z_H, \beta_H, E_H^*) \\ &+ V^C(A_i, Z_i, \beta_i, R_m) + V^N(A_i, Z_i, \beta_i, R_m) \\ &+ V^R(A_i, Z_i, \beta_i, R_m, L) \end{aligned} \quad (1)$$

of the system is calculated as the sum energies of the fragments [the liquid-drop (LD) energy U_i^{LD} plus shell-

correction $\delta U_i^{\text{shell}}$ energy] and energy $V^{\text{int}} = V^C + V^N + V^R$ of the fragment-fragment interaction [15–19]. The interaction potential consists of the Coulomb interaction potential V^C of two uniformly charged ellipsoids, rotational energy V^R , and nuclear interaction potential taken in the double-folding form [30]. The moment of inertia of the DNS formed is calculated in the sticking limit. The excitation energy dependencies of the liquid-drop and shell-correction terms are taken as in Refs. [15–19]. The excitation energy E_{DNS}^* of the scission configuration (DNS) is assumed to be distributed between the fragments proportional to their masses: $E_i^* = E_{\text{DNS}}^* A_i / A_{\text{CN}}$. The deformation-dependent surface tension coefficient is taken as in Ref. [25].

The relative formation and decay probability of the dinuclear system with particular masses, charges, and deformations of the fragments is calculated within the statistical approach as follows [15–19]:

$$\begin{aligned} w(A_i, Z_i, \beta_i, L) &= N_0(2L + 1) \exp \left[-\frac{U(\{A_i, Z_i, \beta_i\}, R_m, L)}{T_{\text{CN}}(L)} \right] \\ &\times \exp \left[-\frac{B_{qf}(\{A_i, Z_i, \beta_i\}, L)}{T_{\text{DNS}}(L)} \right], \end{aligned} \quad (2)$$

where N_0 is the normalization factor. The term $\exp[-B_{qf}/T_{\text{DNS}}]$ describes the decay probability of the dinuclear system in R . The height of barrier B_{qf} is simply taken as $B_{qf} = V^{\text{int}}(R_b, L) - V^{\text{int}}(R_m, L)$ (where $R_b \simeq R_m + 2$ fm is the position of the Coulomb barrier) and has a strong dependence on the charge numbers and deformation parameters of interacting fragments, and angular momentum L . It is smaller for mass/charge symmetric configurations than for asymmetric ones and for highly deformed configurations than for compact (small $\beta_{L,H}$) ones. Because the potential energy contains the repulsive centrifugal part, the value of B_{qf} decreases with increasing angular momentum. For the fissioning nuclei under consideration, the values of B_{qf} are quite large even for the symmetric fragmentations and we do not impose any restriction on the lower limit of B_{qf} or, correspondingly, on the upper

TABLE I. The excitation energies $E_{\text{CN}}^*(L = 0)$ at zero angular momentum as well as the maximum angular momenta of the CN formed in indicated complete fusion reactions.

Reaction	$E_{\text{CN}}^*(L = 0)$ (MeV)	L_{max}
$^{194}\text{Pt}(\alpha, f)$	49	30
$^{36}\text{Ar} + ^{144}\text{Sm} \rightarrow ^{180}\text{Hg}^*$	33.4	$L_{\text{kin}} = 9$
	48	$L_{\text{kin}} = 51$
	65.8	$L_{\text{cr}} = 73$
$^{36}\text{Ar} + ^{154}\text{Sm} \rightarrow ^{190}\text{Hg}^*$	56	$L_{\text{kin}} = 24$
	62.4	$L_{\text{kin}} = 43$
	70.5	$L_{\text{cr}} = 59$
$^{40}\text{Ca} + ^{142}\text{Nd} \rightarrow ^{182}\text{Hg}^*$	33	$L_{\text{kin}} = 10$
	58	$L_{\text{kin}} = 67$
	75	$L_{\text{cr}} = 74$
$^{48}\text{Ca} + ^{154}\text{Sm} \rightarrow ^{202}\text{Pb}^*$	49	$L_{\text{kin}} = 30$
	57	$L_{\text{kin}} = 59$
	95	$L_{\text{cr}} = 91$

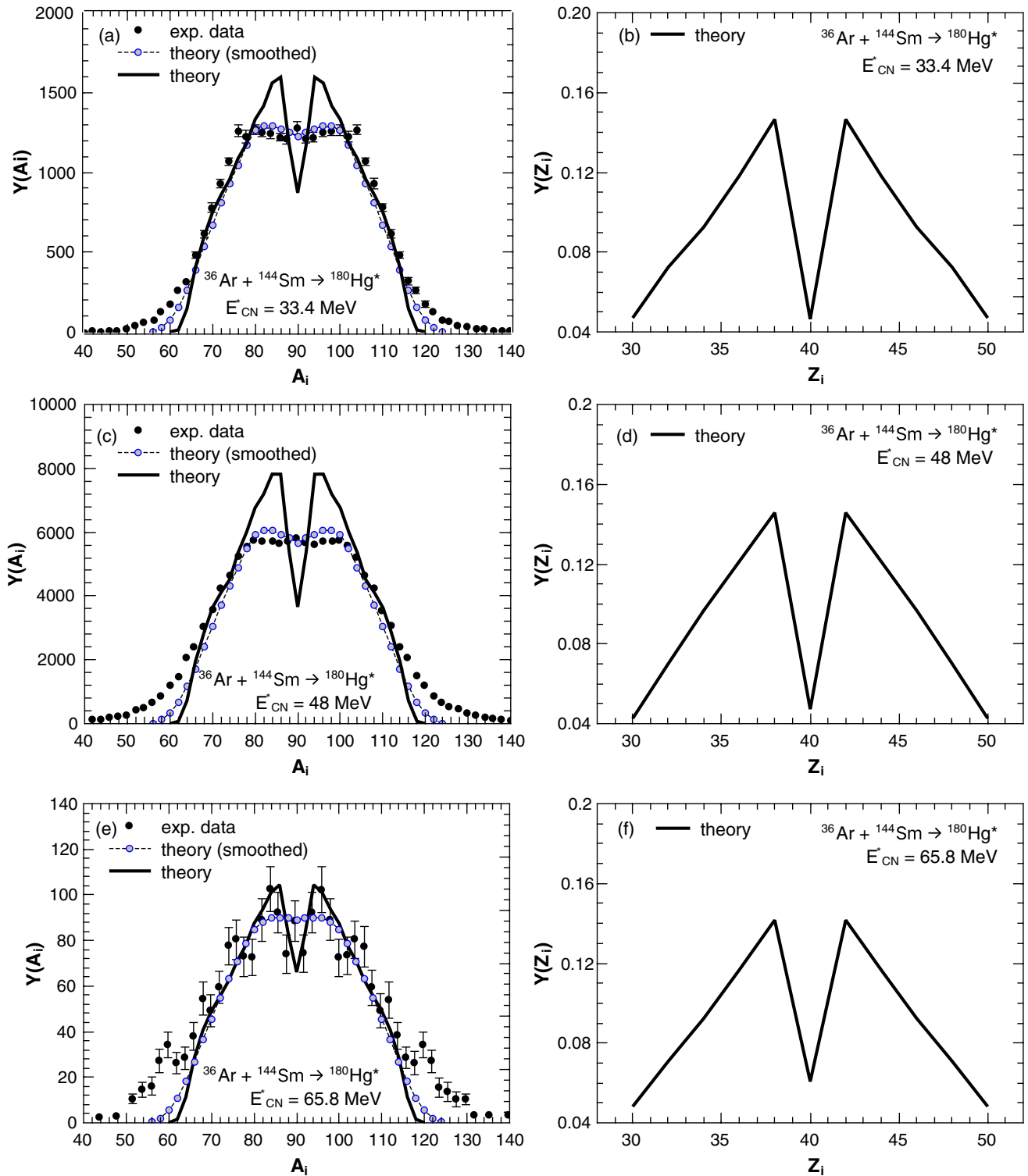


FIG. 1. Calculated mass distributions (thin solid lines) for the fission resulting from the reactions $^{36}\text{Ar} + ^{144}\text{Sm} \rightarrow ^{180}\text{Hg}^*$ at $E_{\text{lab}} = 157$, 175, and 197 MeV compared with the experimental data (closed symbols) [11] (a), (c), (e). The excitation energies of the CN at $L = 0$ are also given. The open symbols represent the calculated mass distributions smoothed with the Gaussian function having the width $\sigma = 2.4$ u. The thick dashed lines connecting the open symbols are for eye guidance. Panels (b), (d), and (f) present the predicted charge distributions for the same reactions.

limits of $\beta_{L,H}$ [15–17]. In Eq. (2), the CN and, respectively, DNS temperatures are calculated as $T_{\text{CN}} = \sqrt{E_{\text{CN}}^*/a}$ and $T_{\text{DNS}} = \sqrt{E_{\text{DNS}}^*/a}$ where $a = A/12 \text{ MeV}^{-1}$ is the level density parameter [26]. Finally, for the calculations of mass and charge distributions the following expressions are obtained:

$$Y(A_i) = \sum_{L=0}^{L_{\text{max}}} \int d\beta_L d\beta_H dZ_i w(A_i, Z_i, \beta_i, L),$$

$$Y(Z_i) = \sum_{L=0}^{L_{\text{max}}} \int d\beta_L d\beta_H dA_i w(A_i, Z_i, \beta_i, L). \quad (3)$$

The value of L is limited by either the kinematic angular momentum L_{kin} or the critical angular momentum L_{cr} in the entrance channel, depending on which one is smaller: $L_{\text{max}} = \min\{L_{\text{kin}}, L_{\text{cr}}\}$ (see Table I). Note that in order to simulate the minimal experimental uncertainties, the mass yields in our paper are smoothed using a Gaussian function with width $\sigma = 0.5 \text{ u}$, unless otherwise specified. The charge yields are not smoothed.

III. CALCULATED RESULTS

To reveal the dependence of the shape of fission-fragment mass distribution on the excitation energy of the fissioning nucleus, we treated the fission of $^{180}\text{Hg}^*$ formed in the complete fusion reaction $^{36}\text{Ar} + ^{144}\text{Sm}$ at bombarding energies $E_{\text{lab}} = 157, 175,$ and 197 MeV (Fig. 1 and Table I) [11]. The corresponding excitation energies of $^{180}\text{Hg}^*$ are $E_{\text{CN}}^* = 33.4, 48,$ and 65.8 MeV , respectively. As seen, the increase of excitation energy and angular momentum in the CN leads to more symmetric mass distribution. This is to be expected, since, on the one hand, with increasing excitation energy the shells “melt” and the system is left with a predominant symmetric mode and, on the other hand, the general effect of the angular momentum is to produce more mass (charge) symmetric fission fragments [31]. Our model describes the

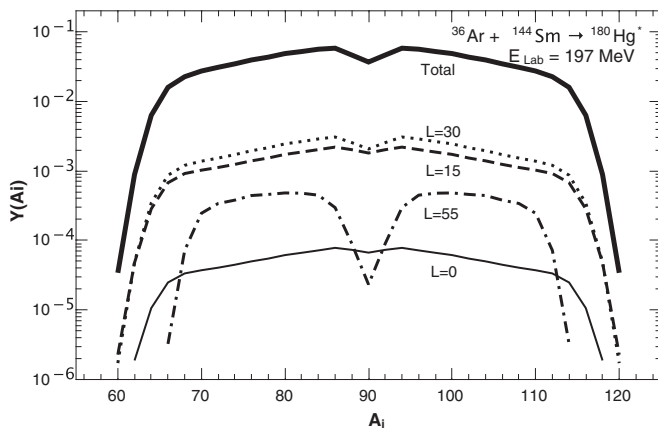


FIG. 2. The relative contributions of indicated angular momenta to the mass distribution (thick solid line) in the case of the $^{36}\text{Ar} + ^{144}\text{Sm} \rightarrow ^{180}\text{Hg}^*$ reaction at $E_{\text{lab}} = 197 \text{ MeV}$ [$E_{\text{CN}}^*(L=0) = 65.8 \text{ MeV}$]. The contribution of all partial waves is shown by the thin solid line.

experimental data rather well; however, the local symmetric minimum is present. If we take into consideration the experimental uncertainty $\sigma = 2.4 \text{ u}$ of mass resolution [11], the measured data are faithfully reproduced (Fig. 1). One can conclude that the finite experimental mass resolution of the fission fragments can have an unwanted effect, severely masking some fine structures of the mass distribution. We might expect that even at large excitation energies and/or angular momenta the mass distribution does not exhibit smooth distributions with plateau. Similar examples can be found in Refs. [6,11,16–19], where at large excitation energies the isotopes of U and Pu displayed asymmetric peaks or a wider plateau than those predicted by the liquid-drop model. So, a direct or an indirect effect of the shell structure is expected even at high excitation energies and angular momenta.

The explanation of the asymmetric mass distribution at high excitation energy can be found by analyzing the relative

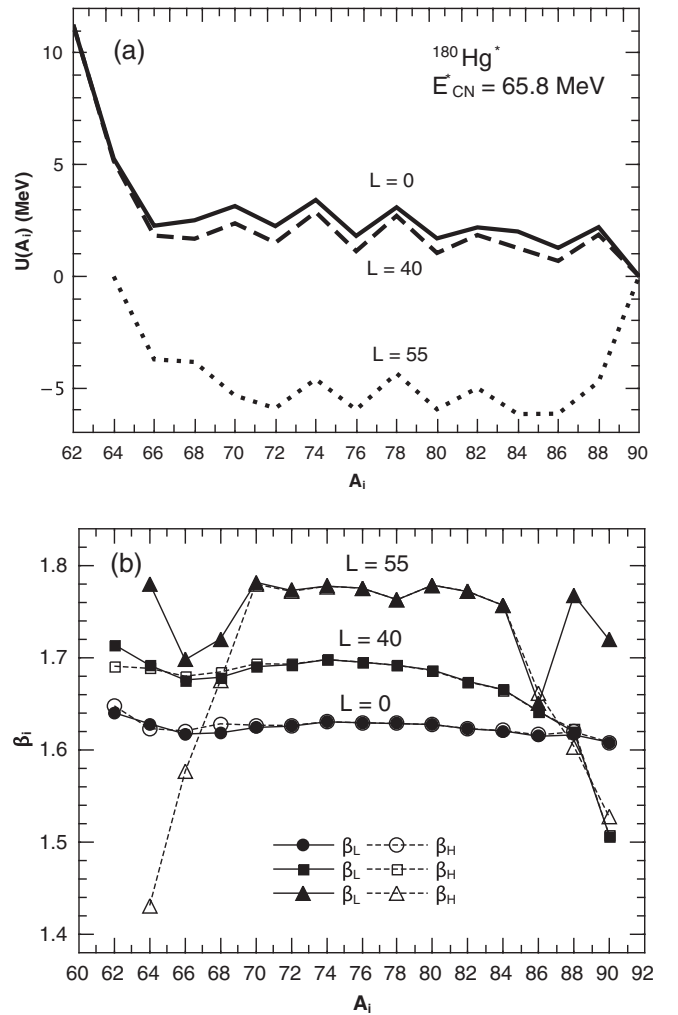


FIG. 3. For the fissioning nucleus $^{180}\text{Hg}^*$, the calculated average potential energy $U(A_i)$ as a function of the mass number of one of the fragments at indicated angular momenta L . (a) The driving potential is normalized such that $U(A_{\text{CN}}/2) = 0$. (b) The calculated average deformations β_H and β_L of the two fragments as functions of their mass numbers at indicated values of L .

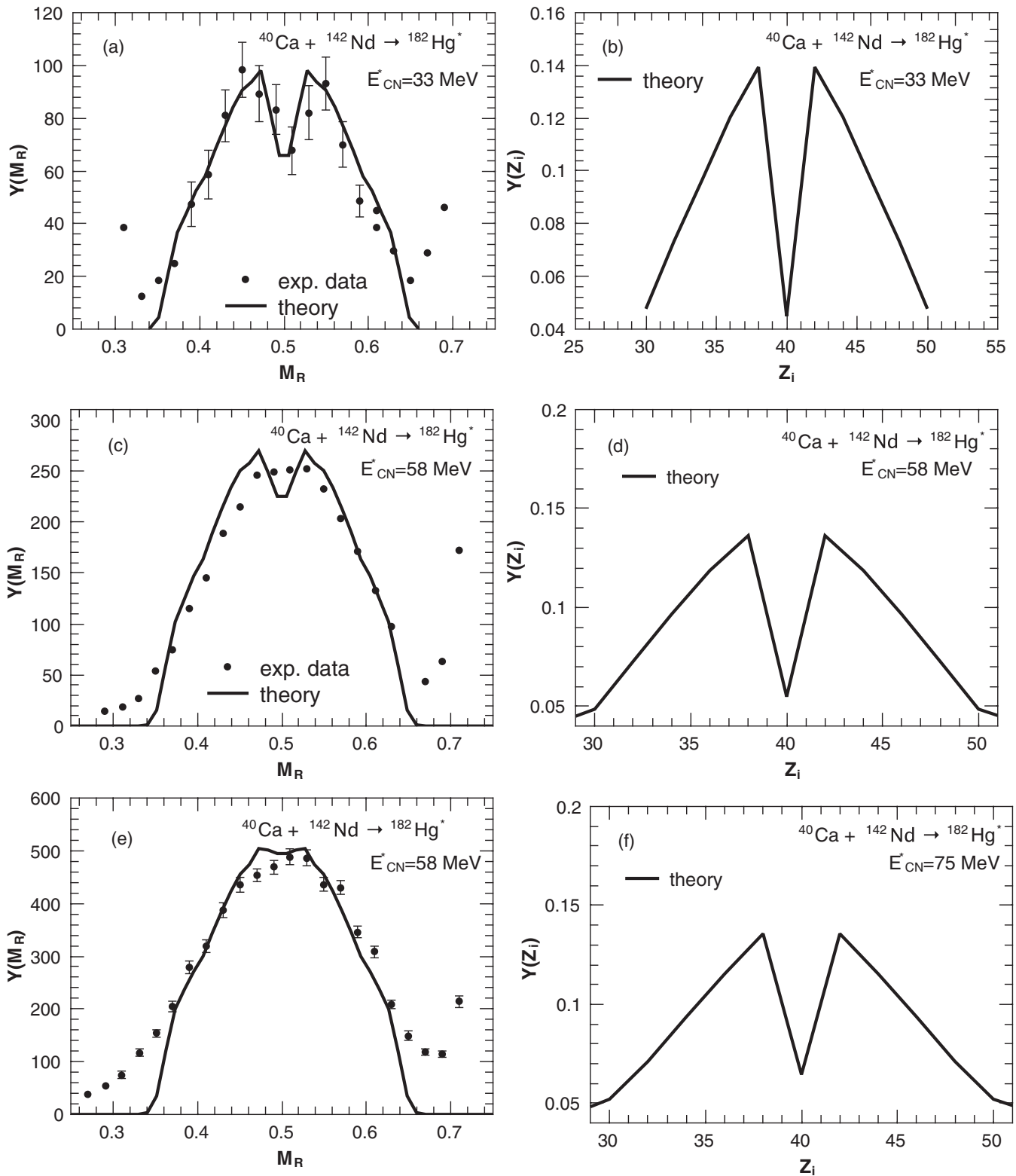


FIG. 4. The same as in Fig. 1, but for the $^{40}\text{Ca} + ^{142}\text{Nd} \rightarrow ^{182}\text{Hg}^*$ reaction at $E_{\text{CN}}^*(L=0) = 33, 58,$ and 75 MeV [panels (a), (c), and (e), respectively]. Here, $M_R = A_i/(A_L + A_H)$ is the fragment mass ratio. In panels (b), (d), and (f) the predicted charge distributions are shown. The experimental data are taken from Ref. [12].

contributions to the mass yields originating from the systems with different angular momenta L . In Fig. 2, the fission-fragment yields originating from fissioning systems with

$L = 0, 15, 30,$ and 55 are separately shown together with their total contribution for the $^{36}\text{Ar} + ^{144}\text{Sm} \rightarrow ^{180}\text{Hg}^*$ reaction at $E_{\text{lab}} = 197$ MeV. At low angular momenta ($L = 0$ and 15)

the yields show the liquid-drop-like behavior. The potential energy in mass asymmetry coordinates is rather smooth due to the large excitation energy. The largest contributions originate from $L = 10\text{--}40$. As the angular momentum increases, the rotational energy increases, leaving the system with less

excitation energy, resulting in stronger shell effects, and therefore a more pronounced structure of the mass yields. Also, larger L values (smaller excitation energies) lead to smaller relative yields and fewer mass-asymmetric configurations available (Fig. 2).

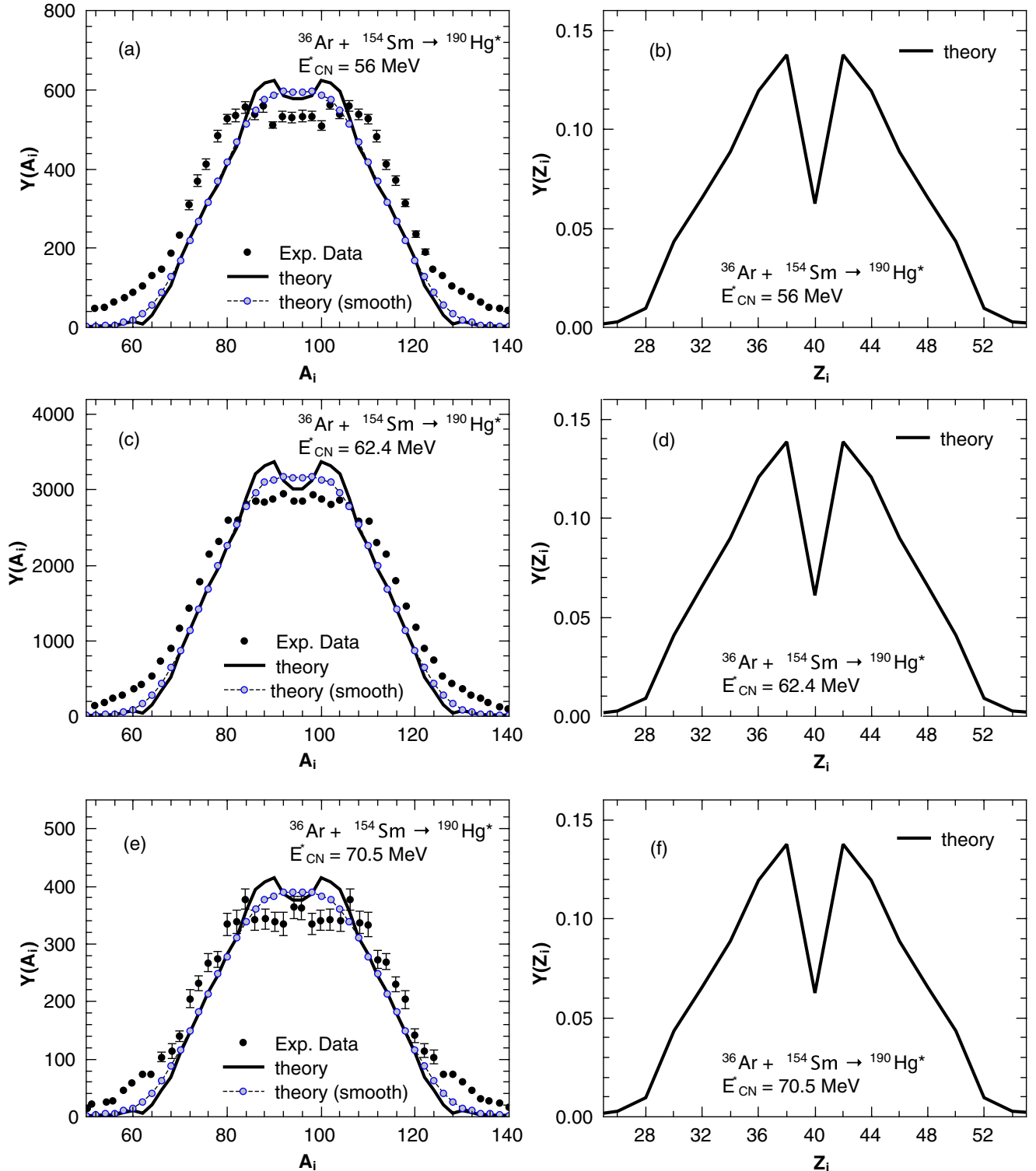


FIG. 5. The same as in Fig. 1, but for the $^{36}\text{Ar} + ^{154}\text{Sm} \rightarrow ^{190}\text{Hg}^*$ reaction, at $E_{\text{CN}}^*(L=0) = 56, 62.4,$ and 70.5 MeV [panels (a), (c), and (e), respectively]. In panels (b), (d), and (f) the predicted charge distributions are shown. The experimental data are taken from Ref. [11].

The effect of excitation energy and angular momentum on the average potential energy as a function of fragment mass number A_i is seen in Fig. 3. The average potential energy of the system as a function of A_i or Z_i at fixed angular momentum L is calculated as

$$U(A_i) = \int d\beta_L d\beta_H dZ_i w(A_i, Z_i, \beta_i, L) U(\{A_i, Z_i, \beta_i\}, R_m, L) \quad (4)$$

or

$$U(Z_i) = \int d\beta_L d\beta_H dA_i w(A_i, Z_i, \beta_i, L) \times U(\{A_i, Z_i, \beta_i\}, R_m, L). \quad (5)$$

The values of U are normalized relative to the average potential energy of the symmetric configuration such that $U(A_i = A_{CN}/2) = 0$ or $U(Z_i = Z_{CN}/2) = 0$. The average values of the fission fragment's deformations are calculated in a similar way and also shown in Fig. 3 for different values of L . For $L = 0$ and 40 the fragment deformations are almost independent of the mass number and equal between two fragments. This is due to the large excitation energy presented in the system. As the angular momentum in the system increases, more elongated configurations become energetically favorable due to the centrifugal part of the potential. At large values of L , large fragment elongation is favorable, but the diminishing excitation energy leads to small deformations of magic nuclei. This can be seen in Fig. 3 at $L = 55$ for $A_H = 116$ (Sn) and $A_L = 90$ (Zr). At these mass numbers, the centrifugal part of the potential becomes large, leading to the maxima in Fig. 3 and, correspondingly, to the minima in the mass yield seen in Fig. 2 at $L = 55$. So, the mass distribution is the sum of low L , almost structureless, distributions and high L distributions which reflect the microscopic shell effects. Note also that, as the value of the angular momentum increases, the excitation energy decreases and at highest L values not all configurations are energetically available.

In Fig. 4, the mass distributions resulting from the $^{40}\text{Ca} + ^{142}\text{Nd} \rightarrow ^{182}\text{Hg}^*$ reaction are compared with available experimental data [12] at excitation energies $E_{CN}^* = 33, 58,$ and 75 MeV of the CN (Table I). As seen, the experimental data [12] are rather well reproduced. One can compare the results in Fig. 4 with those in the fission of $^{180}\text{Hg}^*$ (Fig. 1). If the excitation energies of $^{180,182}\text{Hg}^*$ are approximately the same, the additional two neutrons in $^{182}\text{Hg}^*$ prevent the symmetric fragments from having closed $N_L = N_H = 50$ neutron shells as in the case of $^{180}\text{Hg}^*$. This makes the ratio between the asymmetric maxima and the symmetric minimum for the $^{40}\text{Ca} + ^{142}\text{Nd} \rightarrow ^{182}\text{Hg}^*$ reaction (Fig. 4) smaller than the one for the $^{36}\text{Ar} + ^{144}\text{Sm} \rightarrow ^{180}\text{Hg}^*$ reaction (Fig. 1). For example, one can compare the mass distribution depicted in Fig. 4, where $E_{CN}^*(L = 0) = 58$ MeV, with the one in Fig. 1 with $E_{CN}^*(L = 0) = 65.8$ MeV. Even though the excitation energy is higher in the case of $^{180}\text{Hg}^*$, the peak-to-valley ratio is larger. Note that the values of maximum angular momentum for these two systems are quite similar (see Table I).

The calculated mass distributions from fissioning $^{190}\text{Hg}^*$ formed in the $^{36}\text{Ar} + ^{154}\text{Sm} \rightarrow ^{190}\text{Hg}^*$ reaction are shown in

Fig. 5 and compared with the experimental data at bombarding energies $E_{\text{lab}} = 157, 165,$ and 175 MeV or corresponding excitation energies $E_{CN}^* = 56, 62.4,$ and 70.5 MeV [11] (see Table I). With increasing excitation energy neither the experimental data nor the theoretical results show significant changes in this excitation energy range. This was pointed out in Ref. [11]. However, the mass distribution exhibits much more shallow minima at symmetry than those in the fission of $^{180,182}\text{Hg}^*$. The explanation of this becomes evident if we compare the average potential energy U of the mass number of one fragment at different angular momenta L (Figs. 3 and 6).

In Figs. 1, 4, and 5, the charge distributions in fission of $^{180,182,190}\text{Hg}^*$ are predicted. They have similar features, which are an asymmetric double-peaked nature and a large peak-to-valley ratio at low excitation energies. As the excitation

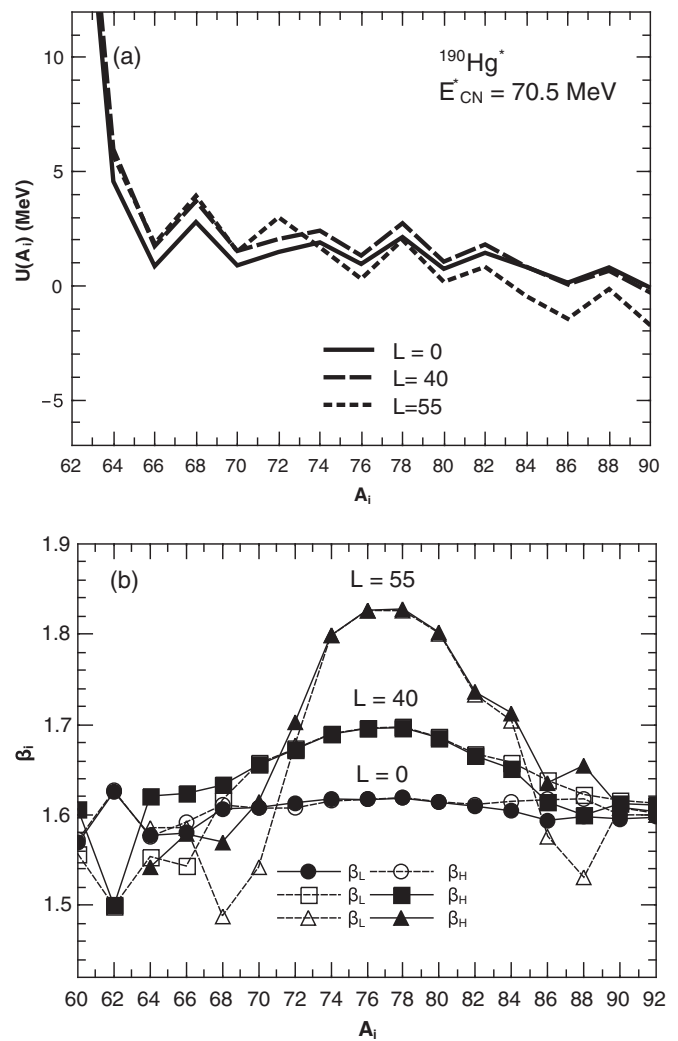


FIG. 6. (a) The calculated average total potential energy $U(A_i)$ as a function of the mass number of one of the fragments at indicated angular momenta L . The driving potential is normalized such that $U(A_{CN}/2) = 0$. (b) The calculated average deformations β_H and β_L of the two fragments as a function of their mass numbers at indicated values of L .

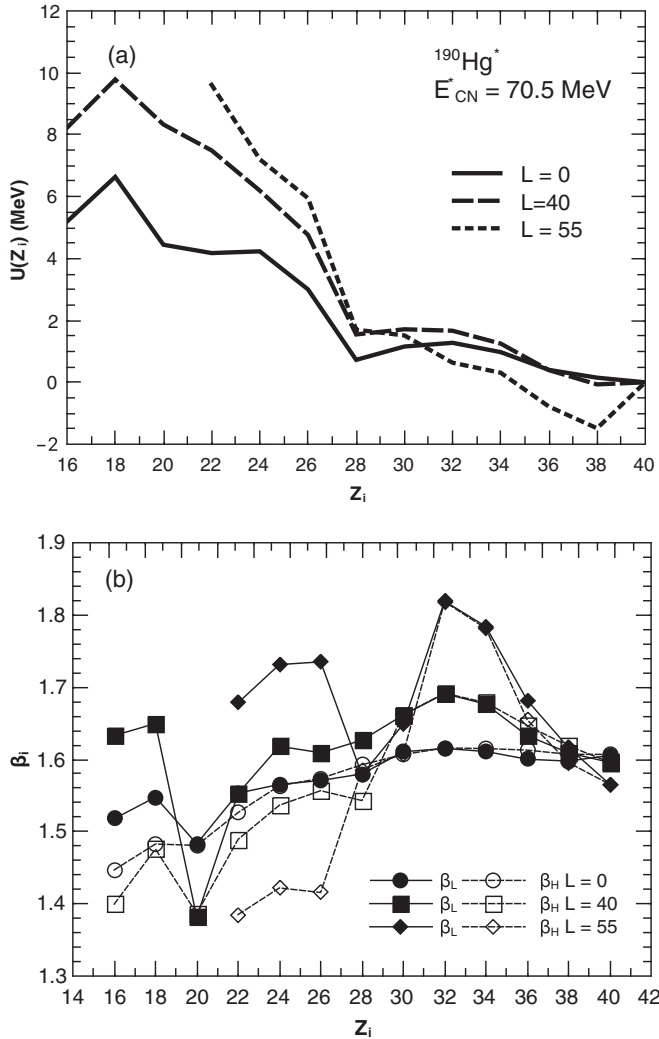


FIG. 7. (a) The calculated average total potential energy $U(Z_i)$ as a function of the charge number of one of the fragments at indicated angular momenta L . The driving potential is normalized such that $U(Z_{\text{CN}}/2) = 0$. (b) The calculated average deformations β_H and β_L of the two fragments as a function of their charge numbers at indicated values of L .

energy and angular momentum of the CN increase this ratio decreases. While the charge distributions in these reactions are quite similar, the mass distributions bear more discrepancies. This is an important observation, because it means that the average N_i/Z_i ratio of the fragments is not constant, and depends on the excitation energy and angular momentum of the fissioning nucleus [9]. The fission of $^{182}\text{Hg}^*$ at $E_{\text{CN}}^* = 75$ MeV (Fig. 4) is quite interesting: it exhibits an almost symmetric mass distribution and a clearly asymmetric charge distribution. This effect can be easily understood on the basis that Sr and Mo nuclei appear in several mass fragmentations with rather large yields. The difference between the mass and charge yields is reflected in different dependencies of the average potential energy on the mass and charge numbers of fragments (Figs. 6 and 7). While $U(A_i)$ (Fig. 6) has a local minimum at $A_L = 90$ and all L considered, the dependence of the average potential energy $U(Z_i)$ does not

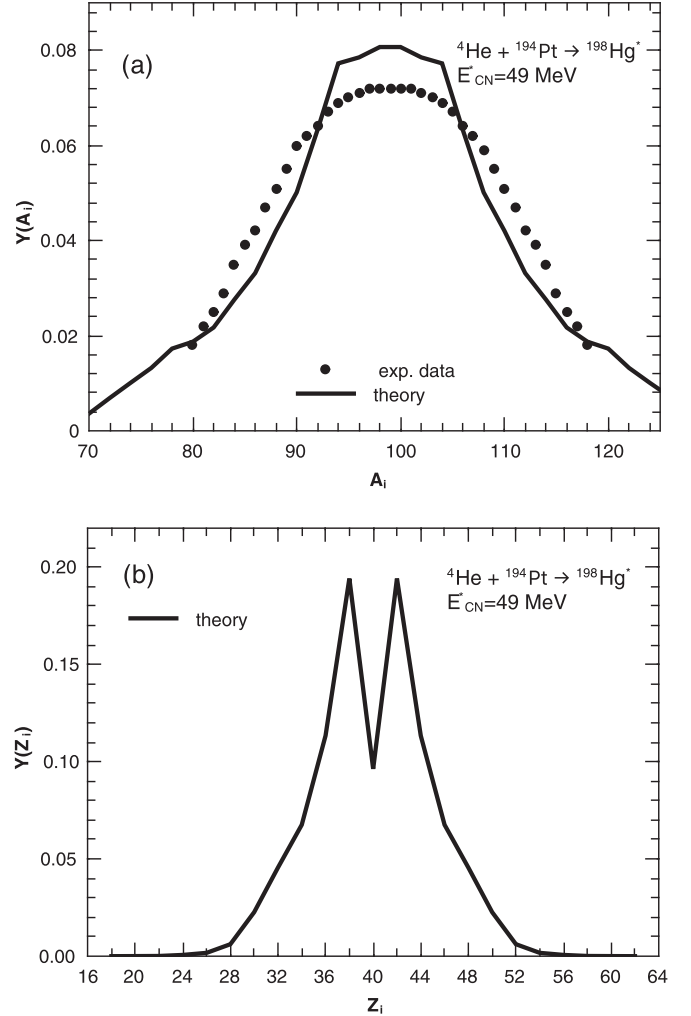


FIG. 8. (a) The experimental (symbols) and calculated (line) mass distributions for the $\alpha + ^{194}\text{Pt} \rightarrow ^{198}\text{Hg}^*$ reaction. (b) The predicted charge distribution for the same reaction. The excitation energy of the CN at $L = 0$ is $E_{\text{CN}}^*(L = 0) = 49$ MeV. The experimental data are taken from Ref. [32].

exhibit a minimum at $Z_{L,H} = 40$. Moreover, at $L = 55$ $U(Z_i)$ has a minimum at $Z_L = 38$ and maximum at $Z_{L,H} = 40$ (Fig. 7).

In Fig. 8, the mass and charge yields in the α -induced fission of ^{194}Pt [the fissioning nucleus is $^{198}\text{Hg}^*$ (Table I)] at $E_{\text{CN}}^* = 49$ MeV are presented and compared with the experimental data [32]. The mass distribution is symmetric in both experiment and theory. The $^{198}\text{Hg}^*$ nucleus shows a mass-symmetric fission which differs from that of $^{180,182,190}\text{Hg}^*$. The predicted charge distribution, however, is asymmetric, with a peak-to-valley ratio of ≈ 2 . However, this ratio is smaller than those in the fission of $^{180,182,190}\text{Hg}^*$.

In the $^{48}\text{Ca} + ^{154}\text{Sm} \rightarrow ^{202}\text{Pb}^*$ reaction at $E_{\text{CN}}^* = 49, 57,$ and 95 MeV (Fig. 9 and Table I), the experimental data [33] are well reproduced. The fission of $^{202}\text{Pb}^*$ exhibits clearly symmetric mass and charge distributions. These distributions are symmetric at all excitation energies. Our conclusion about the shape of the mass and charge distributions is not sensitive

to the variation of the level density parameter a . In the experiment at the lowest energy, asymmetric shoulders are observed. However, the latter are related to the dynamical quasifission process [34–40], which is outside the scope of

the present paper. Note that in the experiment as well as in the theory the distributions become wider with increasing excitation, because more mass-asymmetric configurations are reached. This effect can be experimentally investigated.

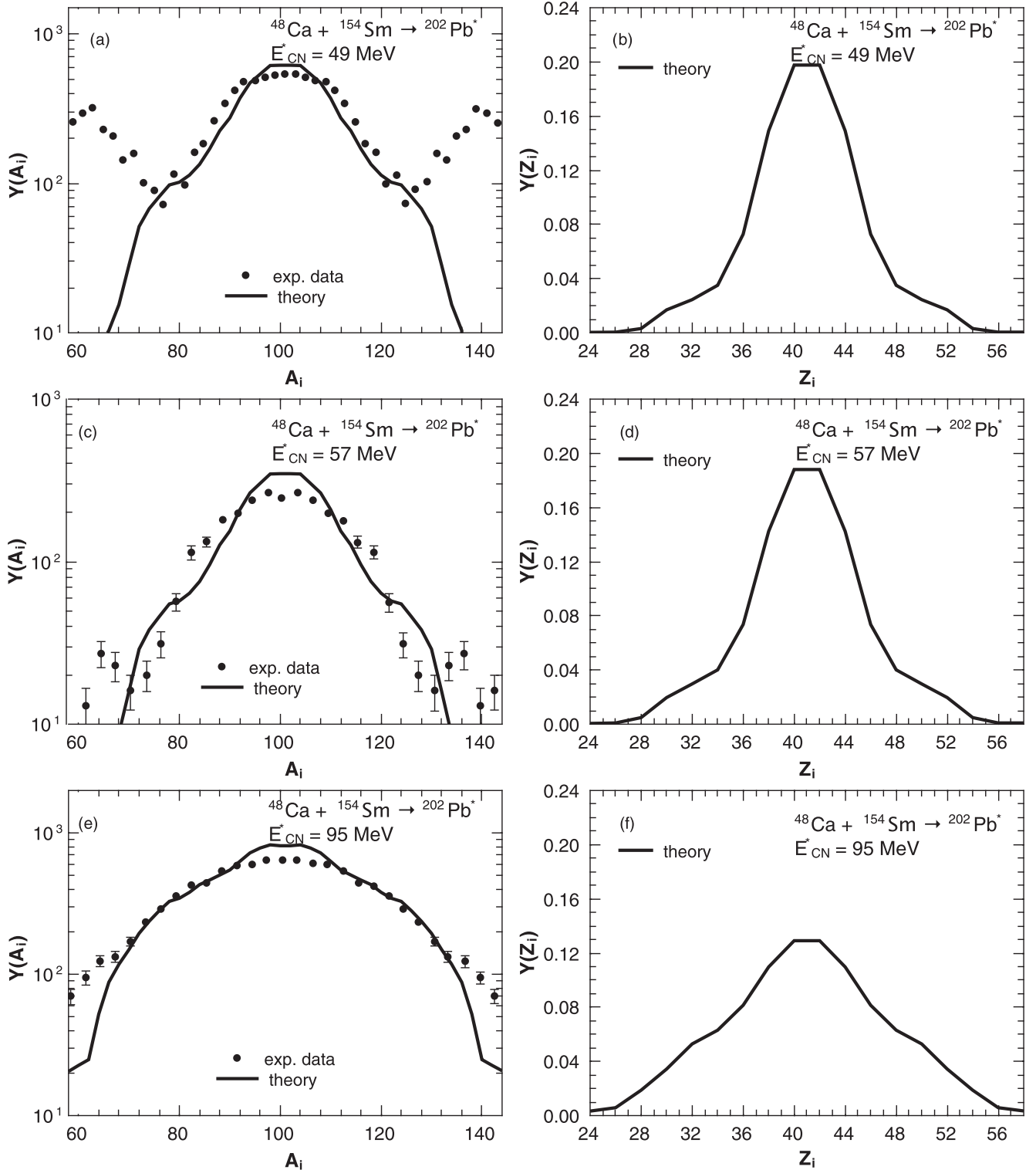


FIG. 9. (a), (c), (e) The same as in Fig. 1, but for the $^{48}\text{Ca} + ^{154}\text{Sm} \rightarrow ^{202}\text{Pb}^*$ reaction at indicated excitation energies $E_{\text{CN}}^*(L=0) = 49, 57,$ and 95 MeV. (b), (d), (f) The predicted charge distributions are shown. The experimental data are taken from Ref. [33].

IV. CONCLUSIONS

In summary, the mass distributions of fission fragments of several fissioning nuclei $^{180,182,190,198}\text{Hg}^*$ formed in the complete fusion reactions $^{36}\text{Ar} + ^{144}\text{Sm}$, $^{40}\text{Ca} + ^{142}\text{Nd}$, $^{36}\text{Ar} + ^{154}\text{Sm}$, $\alpha + ^{194}\text{Pt}$, and $^{48}\text{Ca} + ^{154}\text{Sm}$ were calculated and compared with the existing experimental data. The obtained dependencies of the mass distributions on excitation energy of CN ($E_{\text{CN}}^* \sim 33\text{--}95$ MeV) are in a good agreement with the experimental data. The low angular momentum L values contribute to the total yields leading to rather smooth mass distribution, while the high L values contribute to the total yields preserving the microscopic shell effects. Their combined effect is to preserve the structure of the distribution found usually at low excitation energies and angular momenta, while still weakly increasing the weight of symmetric configurations in the total yields. With increasing bombarding energy the symmetric yields increase up to the maximum at critical angular momentum L_{cr} , after which, as excitation energy increases, the theoretical mass and charge distributions widen. The charge distribution was predicted to be less affected by excitation energy and angular momentum than the mass distribution.

For the fissioning nuclei $^{180,182,190,198}\text{Hg}^*$, the asymmetric charge distributions were predicted up to high excitation energy. In contrast, for $^{202}\text{Pb}^*$, the symmetric charge distribution was obtained. The interesting cases found are the fissions of $^{182}\text{Hg}^*$ at $E_{\text{CN}}^* = 75$ MeV and $^{198}\text{Hg}^*$ at $E_{\text{CN}}^* = 49$ MeV. They exhibit a symmetric mass distribution (within the mass resolution of measurements), while the predicted charge distribution has a pronounced double-peaked structure. For the fissioning nuclei $^{180,182,190,198}\text{Hg}^*$, the average N_i/Z_i ratio of the fragments is not constant, and depends on the excitation energy and angular momentum of the fissioning nucleus. Note that, for the fissioning actinides, a similar effect was experimentally observed in Ref. [9].

ACKNOWLEDGMENTS

This work was partially supported by the Romania-JINR(Dubna) Cooperation Programme, the Russian Foundation for Basic Research (Grant No. 17-52-12015), and Deutsche Forschungsgemeinschaft. The work of N.V.A. was supported by a Tomsk Polytechnic University Competitiveness Enhancement Program grant.

-
- [1] A. N. Andreyev, M. Huyse, and P. Van Duppen, *Rev. Mod. Phys.* **85**, 1541 (2013).
- [2] U. Brosa, S. Grossmann, and A. Müller, *Phys. Rep.* **197**, 167 (1990).
- [3] I. V. Ryzhov *et al.*, *Phys. Rev. C* **83**, 054603 (2011).
- [4] V. Simukhin, Ph.D. thesis, Uppsala University, 2010; I. V. Ryzhov *et al.*, *J. Korean Phys. Soc. C* **59**, 1864 (2011); V. Simukhin *et al.*, *Nucl. Data Sheets* **119**, 331 (2014).
- [5] J. King *et al.*, *Eur. Phys. J. A* **53**, 238 (2017).
- [6] R. Léguillon *et al.*, *Phys. Lett. B* **761**, 125 (2016); K. Hirose *et al.*, *Phys. Rev. Lett.* **119**, 222501 (2017).
- [7] H. Naik *et al.*, *Phys. Rev. C* **85**, 039905 (2012); **85**, 024623 (2012); *Nucl. Phys. A* **913**, 185 (2013); **941**, 16 (2015); **952**, 100 (2016).
- [8] A. Deppman, E. Andrade-II, V. Guimarães, G. S. Karapetyan, and N. A. Demekhina, *Phys. Rev. C* **87**, 054604 (2013); A. Deppman, E. Andrade-II, V. Guimarães, G. S. Karapetyan, A. R. Balabekyan, and N. A. Demekhina, *ibid.* **88**, 024608 (2013); A. Deppman *et al.*, *ibid.* **88**, 064609 (2013).
- [9] D. Ramos *et al.*, *Phys. Rev. C* **97**, 054612 (2018); **99**, 024615 (2019).
- [10] D. Ramos *et al.*, *Phys. Rev. Lett.* **123**, 092503 (2019).
- [11] K. Nishio *et al.*, *Phys. Lett. B* **748**, 89 (2015).
- [12] E. Prasad *et al.*, *Phys. Rev. C* **91**, 064605 (2015).
- [13] I. Tsekhanovich *et al.*, *Phys. Lett. B* **790**, 583 (2019).
- [14] H. Pașca, A. V. Andreev, G. G. Adamian, and N. V. Antonenko, *Eur. Phys. J. A* **54**, 104 (2018).
- [15] H. Pașca, A. V. Andreev, G. G. Adamian, and N. V. Antonenko, *Phys. Lett. B* **760**, 800 (2016).
- [16] H. Pașca, A. V. Andreev, G. G. Adamian, and N. V. Antonenko, *Phys. Rev. C* **94**, 064614 (2016).
- [17] H. Pașca, A. V. Andreev, G. G. Adamian, and N. V. Antonenko, *Phys. Rev. C* **97**, 034621 (2018).
- [18] H. Pașca, A. V. Andreev, G. G. Adamian, and N. V. Antonenko, *Nucl. Phys. A* **969**, 226 (2018).
- [19] H. Pașca, A. V. Andreev, G. G. Adamian, and N. V. Antonenko, *Phys. Rev. C* **99**, 064611 (2019).
- [20] B. D. Wilkins, E. P. Steinberg, and R. R. Chasman, *Phys. Rev. C* **14**, 1832 (1976).
- [21] T. Matsuse, C. Beck, R. Nouicer, and D. Mahboub, *Phys. Rev. C* **55**, 1380 (1997).
- [22] S. J. Sanders, A. Szanto de Toledo, and C. Beck, *Phys. Rep.* **311**, 487 (1999).
- [23] S. Panebianco, J.-L. Sida, H. Goutte, J.-F. Lemaître, N. Dubray, and S. Hilaire, *Phys. Rev. C* **86**, 064601 (2012).
- [24] M. Caamaño *et al.*, *Phys. Rev. C* **92**, 034606 (2015).
- [25] A. V. Andreev, G. G. Adamian, N. V. Antonenko, S. P. Ivanova, and W. Scheid, *Eur. Phys. J. A* **22**, 51 (2004); A. V. Andreev, G. G. Adamian, N. V. Antonenko, and S. P. Ivanova, *ibid.* **26**, 327 (2005); A. V. Andreev, G. G. Adamian, and N. V. Antonenko, *Phys. Rev. C* **86**, 044315 (2012); A. V. Andreev, G. G. Adamian, N. V. Antonenko, and A. N. Andreyev, *ibid.* **88**, 047604 (2013).
- [26] G. G. Adamian, N. V. Antonenko, and W. Scheid, *Clusters in Nuclei*, Lecture Notes in Physics Vol. 848, edited by Christian Beck (Springer-Verlag, Berlin, 2012), Vol. 2, p. 165.
- [27] H. Pașca, A. V. Andreev, G. G. Adamian, N. V. Antonenko, and Y. Kim, *Phys. Rev. C* **93**, 054602 (2016); H. Pașca, *EPJ Web Conf.* **107**, 07003 (2016).
- [28] H. Pașca, A. V. Andreev, G. G. Adamian, and N. V. Antonenko, *Eur. Phys. J. A* **52**, 369 (2016).
- [29] J. Maruhn and W. Greiner, *Z. Phys.* **251**, 431 (1972).
- [30] G. G. Adamian *et al.*, *Int. J. Mod. Phys. E* **5**, 191 (1996).
- [31] Sh. A. Kalandarov, G. G. Adamian, N. V. Antonenko, and W. Scheid, *Phys. Rev. C* **82**, 044603 (2010); **83**, 054611 (2011); **84**, 064601 (2011).

- [32] M. G. Itkis *et al.*, *Sov. J. Nucl. Phys.* **52**, 601 (1990); **53**, 757 (1991).
- [33] G. N. Knyazheva *et al.*, *Phys. Rev. C* **75**, 064602 (2007).
- [34] H. Q. Zhang, C. L. Zhang, C. J. Lin, Z. H. Liu, F. Yang, A. K. Nasirov, G. Mandaglio, M. Manganaro, and G. Giardina, *Phys. Rev. C* **81**, 034611 (2010).
- [35] G. Mandaglio, G. Giardina, A. K. Nasirov, and A. Sobiczewski, *Phys. Rev. C* **86**, 064607 (2012).
- [36] A. K. Nasirov, K. Kim, G. Mandaglio, G. Giardina, A. I. Muminov, and Y. Kim, *Eur. Phys. J. A* **49**, 147 (2013).
- [37] K. Kim, Y. Kim, A. K. Nasirov, G. Mandaglio, and G. Giardina, *Phys. Rev. C* **91**, 064608 (2015).
- [38] G. Mandaglio, A. Anastasi, F. Curciarello, G. Fazio, G. Giardina, and A. K. Nasirov, *Phys. Rev. C* **98**, 044616 (2018).
- [39] G. Mandaglio, A. K. Nasirov, A. Anastasi, F. Curciarello, G. Fazio, and G. Giardina, *Nucl. Phys. A* **979**, 204 (2018).
- [40] A. K. Nasirov, B. M. Kayumov, G. Mandaglio, G. Giardina, K. Kim, and Y. Kim, *Eur. Phys. J. A* **55**, 29 (2019).

Correction: The previously published Figure 3 was a duplicate of Figure 6 and has been replaced with the correct figure.